

# 3D Vessel Reconstruction from Sparse-View Dynamic DSA Images via Vessel Probability Guided Attenuation Learning

Zhentao Liu, Huangxuan Zhao, Wenhui Qin, Zhenghong Zhou, Xinggang Wang, Wenping Wang, *Fellow, IEEE*, Xiaochun Lai, Chuansheng Zheng, Dinggang Shen, *Fellow, IEEE*, Zhiming Cui

arXiv:2405.10705v1 [eess.IV] 17 May 2024

**Abstract**—Digital Subtraction Angiography (DSA) is one of the gold standards in vascular disease diagnosing. With the help of contrast agent, time-resolved 2D DSA images deliver comprehensive insights into blood flow information and can be utilized to reconstruct 3D vessel structures. Current commercial DSA systems typically demand hundreds of scanning views to perform reconstruction, resulting in substantial radiation exposure. However, sparse-view DSA reconstruction, aimed at reducing radiation dosage, is still underexplored in the research community. The dynamic blood flow and insufficient input of sparse-view DSA images present significant challenges to the 3D vessel reconstruction task. In this study, we propose to use a time-agnostic vessel probability field to solve this problem effectively. Our approach, termed as vessel probability guided attenuation learning, represents the DSA imaging as a complementary weighted combination of static and dynamic attenuation fields, with the weights derived from the vessel probability field. Functioning as a dynamic mask, vessel probability provides proper gradients for both static and dynamic fields adaptive to different scene types. This mechanism facilitates a self-supervised decomposition between static backgrounds and dynamic contrast agent flow, and significantly improves the reconstruction quality. Our model is trained by minimizing the disparity between synthesized projections and real captured DSA images. We further employ two training strategies to improve our reconstruction quality: (1) coarse-to-fine progressive training to achieve better geometry and (2) temporal perturbed rendering loss to enforce temporal consistency. Experimental results have demonstrated superior quality on both 3D vessel reconstruction and 2D view synthesis.

**Index Terms**—DSA image, Sparse-view reconstruction, Vessel probability field, Attenuation field

## I. INTRODUCTION

Zhentao Liu, Wenhui Qin, Xiaochun Lai, Dinggang Shen, and Zhiming Cui are with the School of Biomedical Engineering & State Key Laboratory of Advanced Medical Materials and Devices, ShanghaiTech University, Shanghai, 201210, China. Dinggang Shen is also with Shanghai United Imaging Intelligence Co., Ltd., Shanghai, 200230, China, and Shanghai Clinical Research and Trial Center, Shanghai, 201210, China. (e-mail: \{liuzht2022, qinwh, laixch, dgshen, cuizhm\}@shanghaitech.edu.cn).

Huangxuan Zhao and Chuansheng Zheng are with the Department of Radiology, Union Hospital, Tongji Medical College, Huazhong University of Science and Technology, Wuhan, 430022, China. (e-mail: \{zhao\_huangxuan, hqzcsxh\}@sina.com).

Zhenghong Zhou and Xinggang Wang are with the School of Electronic Information and Communications, Huazhong University of Science and Technology, Wuhan, 430074, China. (e-mail: \{zhouzhust, xgwang\}@hust.edu.cn).

Wenping Wang is with the Department of Computer Science & Engineering, Texas A&M University, USA. (e-mail: wenping@tamu.edu).

DIGITAL subtraction angiography (DSA) plays a vital role in vascular disease diagnosis. The clinical applications for DSA include evaluations of arteriovenous malformation (AVM), arteriovenous fistula (AVF), intracranial aneurysms, atherosclerotic occlusive disease, and etc. [1]–[4]. DSA imaging process is illustrated in Fig. 1. The patient undergoes two rotational X-ray scans at identical positions. The first scan is performed before the injection of contrast agent (mask run), and the second scan is conducted after injection (fill run). Following this, the DSA sequence is generated by subtracting the X-ray images acquired during the fill run from those taken during the mask run in the logarithmic domain. This process highlights the blood flow information marked by the contrast agent while removing other irrelevant tissues. Each DSA image captures a particular blood flow state as the contrast agent gradually fills the vessels. To achieve a holistic understanding of vessel anatomy, the DSA sequence is then utilized to reconstruct 3D vascular structures. However, DSA reconstruction presents a significant challenge due to the dynamic imaging nature, showcasing varying blood flow states at different timestamps.

In current commercial DSA systems, vessel reconstruction still relies on the traditional FDK (Feldkamp, Davis and Kress) algorithm [5], [6], typically requiring hundreds of scanning views to produce high quality images without artifacts. Such large number of X-ray projections induces significant radiation exposure for both patients and radiographers. Thus, there is a pressing need to sparsify scanned views to reduce radiation dosage. However, sparse-view DSA reconstruction that aims to reconstruct high quality 3D vascular structures from a decreased number of X-ray views, is still underexplored in the research community.

With the advancement of deep learning, some attempts have been made to apply convolutional neural networks (CNNs) for sparse-view 3D Cone Beam Computed Tomography (CBCT) and DSA reconstructions on simulated datasets [7]–[12]. They apply the Digitally Reconstruction Radiography (DRR) [13], [14] technique to simulate multi-view X-ray projections from static 3D data for reconstruction. However, these methods are not well-suited for the dynamic DSA images collected in clinical settings. Recently, Neural Radiance Field (NeRF) [15] is becoming a promising technique for high quality novel view synthesis and 3D/4D reconstruction. Several existing CBCT reconstruction methods, such as NeAT [16], NAF [17], and SNAF [18], have utilized the NeRF-based optimization

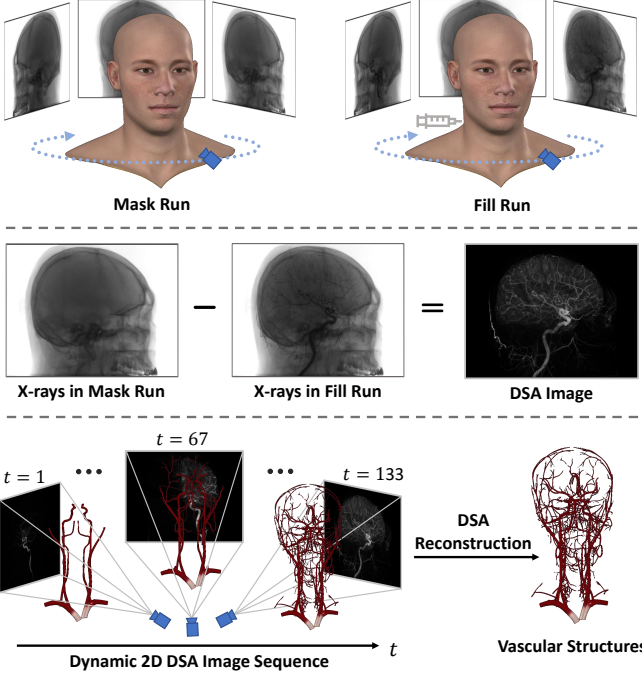


Fig. 1. DSA imaging and reconstruction. DSA imaging process involves two rotational X-ray scans at identical positions: the first one before the injection of contrast agent (mask run) and the second one after injection (fill run). Subsequently, 2D DSA images are derived by subtracting X-ray images taken during fill run from those captured during mask run. This process selectively highlights the dynamic blood flow information marked by the contrast agent while removing other irrelevant tissues. The dynamic 2D DSA image sequence will be utilized to reconstruct the 3D vascular structures.

frameworks and have shown promising results. But they are also primarily designed for static CBCT scans without temporal modeling, limiting their application to dynamic DSA reconstruction. Notably, TiAVox [19] stands out as a relevant work, extending DVGO [20] from temporal dimension and employing learnable 4D voxel grids to recover DSA scanning process. However, majority of the scanned scene is static, directly storing static points in 4D voxel grids leads to severe model storage waste. Since each of them will occupy multiple voxels with an identical value for a multi-frame sequence. As a result, its reconstruction quality often falls short of satisfaction.

In this study, we aim to address two primary challenges in sparse-view dynamic DSA reconstruction. (1) We seek to effectively model the dynamic nature of DSA imaging. (2) We strive to reduce the number of required scanning views while maintaining high reconstruction quality. In fact, DSA imaging inherently possesses a strong prior knowledge. The vessels are static during scanning process, severing as time-independent envelop with dynamic contrast agent flowing through. By harnessing this key observation, we propose to use a time-agnostic vessel probability field to model dynamic DSA imaging effectively. Our approach, termed as vessel probability guided attenuation learning, represents the DSA imaging as a complementary weighted combination of static and dynamic attenuation fields, with the weights derived from the vessel probability field. A high vessel probability  $p$  indicates the presence of vessels, often associated with dynamic flows at that point. This assigns a higher weight  $p$

to the dynamic attenuation field and a lower weight  $1 - p$  to the static one. As a result, during back-propagation, the loss gradients from this point primarily modify the parameters of dynamic field, leaving the static field unaffected. This ensures that dynamic properties will be mainly stored in the dynamic field. Conversely, a low vessel probability suggests static backgrounds dominate at that point, resulting in the reverse weighting scenario. The loss gradients chiefly modify the parameters of static field without disrupting dynamic field, ensuring static properties are mainly stored in the static field. Functioning as a dynamic mask, vessel probability provides proper gradients for both static and dynamic fields adaptive to different scene types. This enables static and dynamic fields to accurately capture static backgrounds and dynamic contrast flow respectively, without interference with each other. It facilitates a self-supervised static-dynamic decomposition and significantly improves the reconstruction quality. We train our model by minimizing the discrepancy between synthesized projections and real captured DSA images. Furthermore, we employ two training strategies to enhance reconstruction quality: (1) coarse-to-fine progressive training to achieve better geometry, and (2) temporal perturbed rendering loss to enforce temporal consistency. Our approach simultaneously enables high-quality 3D vessel reconstruction and 2D view synthesis as demonstrated in the experimental results.

## II. RELATED WORKS

### A. Neural Radiance Field

Neural Radiance Field (NeRF) [15] has rapidly progressed in the field of computer vision, particularly excelling in novel view synthesis and 3D/4D reconstruction. The core concept is to use differentiable volumetric rendering in combination with Implicit Neural Representation (INR) through Multi-layer Perceptrons (MLPs) to learn the density and radiance distribution of a 3D scene [21]. By leveraging the self-consistency between different viewpoints, we can effectively capture the relationship between a 3D scene and its 2D images. Currently, NeRF has been extended from various aspects, including acceleration [20], [22], [23], regularization [24]–[26], surface reconstruction [27]–[29], anti-aliasing [30]–[33], and dynamics [34]–[37]. Of these, the dynamic NeRF is particularly relevant to our DSA reconstruction task. And it could be mainly divided into two categories: canonical-mapping volume rendering [34], [35] and time-aware volume rendering [36], [37]. In our DSA scanning context, the canonical space assumption is not applicable due to the constant changing of blood flow states in different frames. Therefore, our proposed method in this study is based on time-aware volume rendering which directly encoding the temporal dimension.

NeRF techniques have been widely applied in sparse-view CBCT reconstruction task [16]–[18], and achieve commendable results. Instead of learning a radiance field in natural scenes, they try to optimize an attenuation field to reconstruct the 3D CBCT image. However, all of them are designed for static CBCT scans, which make them unsuitable for dynamic DSA reconstruction. TiAVox [19] stands out as the most relevant work. It makes use of learnable 4D voxel grids to

recover the dynamic DSA imaging process, aligning with the category of time-aware volume rendering.

### B. DSA Reconstruction

FDK algorithm [5], [6] is the most widely utilized reconstruction method in current DSA scanning systems. After decades of development, current DSA systems have significantly enhanced the FDK algorithm, enabling it to produce high-quality vascular reconstructions from dynamic DSA images. However, it usually requires hundreds of scanning views (*e.g.*, 133 views in this study) to provide reliable reconstruction quality, leading to considerable radiation exposure. With the advance of deep learning, Zhao *et al.* [12] applies CNNs-based deep learning framework for sparse-view DSA reconstruction using self-supervised projection loss. It employs DRR technique to simulate multi-view static projections from well-reconstructed 3D vessel data obtained via the DSA system, and then performs reconstruction. However, this procedure does not meet our needs for dynamic DSA imaging in practical settings. TiAVox adopts dynamic NeRF techniques for sparse-view DSA reconstruction. It extends DVGO [20] in temporal dimension but does not consider inter-frame relationship in DSA sequence. As discussed in Introduction, the redundant static points storage leads to significant model capacity waste. Additionally, the memory overhead arising from its fully explicit grid representation usually leads to a compromise in spatio-temporal resolution, further limiting its model capacity. In fact, dynamic DSA sequence has strong shared information across different frames, *i.e.*, the inherent vessel structures remain static during scanning process. In this study, we propose to use time-agnostic vessel probability field to model the DSA imaging process effectively, and achieve excellent results on both 3D vessel reconstruction and 2D view synthesis.

## III. METHOD

In this section, we first introduce DSA imaging in Sec. III-A. Following that, we delve into our methodology, *i.e.*, vessel probability guided attenuation learning, in Sec. III-B. Our training strategies, including coarse-to-fine progressive training and temporal perturbed rendering loss, will be illustrated in Sec. III-C. Finally, the vascular structures can be reconstructed by inferring our trained model as described in Sec. III-D.

### A. DSA Imaging

1) *DSA Imaging Process:* As illustrated in Fig. 1, DSA imaging process involves two rotational X-ray scans for a patient. The first scan, termed as the mask run, is conducted before the injection of the contrast agent. The second scan, referred to as the fill run, is performed after a few seconds of the injection. During both scans, the X-ray source rotates along a predefined arc-shaped trajectory around the patient with uniform angular spacing. On the opposite side, a 2D detector captures multi-view projections of the body, such as the head and neck. For both X-ray sequences, images with the same sequential number are captured at the same rotational

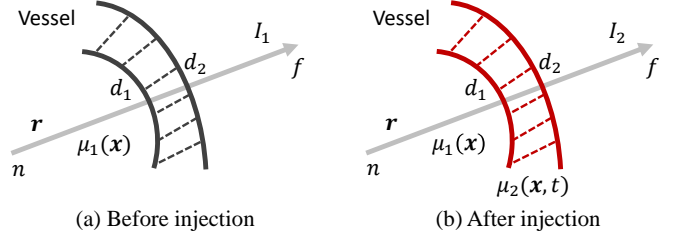


Fig. 2. X-ray attenuation process for cases (a) before injection and (b) after injection of contrast agent.

angle, ensuring consistent positioning. Different tissues in the body absorb X-rays to varying extents, and this absorption rate is termed as “attenuation coefficient”, which is always non-negative. The key distinction between these two X-ray scans lies in the notably increased attenuation in the vessel area due to the injected contrast agent of the fill run. Subsequently, the X-ray images acquired during the fill run are subtracted from those taken during the mask run in logarithmic domain. This subtraction process effectively removes irrelevant tissues, such as bones and muscles, resulting in DSA images that exclusively capture blood flow information as highlighted by the contrast agent.

For illustrative purposes, we select a subset of DSA images for demonstration in Fig. 1, specifically at timestamps  $t = 1, 67$  and  $133$ , from the complete sequence of  $133$  frames. Since the fill run starts after a few seconds of the injection, the first DSA frame ( $t = 1$ ) already shows some initial blood flow information at cervical artery. It is clear that each frame of DSA sequence captures a particular blood flow state as the contrast agents gradually flow through the vessels. Such dynamic nature of DSA images arises a significant challenge to the reconstruction task.

2) *DSA Imaging Formulation:* As illustrated in Fig. 2, in the scenario before the contrast agent injection, the attenuation coefficient across the entire environment is denoted as  $\mu_1(\mathbf{x}), \mathbf{x} \in \mathbb{R}^3$ . Consider an incident X-ray path represented by  $\mathbf{r}(s) = \mathbf{o} + s\mathbf{d} \in \mathbb{R}^3$ . Here  $\mathbf{o} \in \mathbb{R}^3$  denotes the X-ray source position,  $\mathbf{d} \in \mathbb{R}^3$  is its direction, and  $s$  is the non-negative scaling parameter. The X-ray attenuation process along this X-ray path can be expressed according to Beer’s Law [38]:

$$I_1(\mathbf{r}) = I_0(\mathbf{r}) \exp \left( - \int_n^f \mu_1(\mathbf{r}(s)) ds \right) \quad (1)$$

where  $I_0(\mathbf{r})$  represents the initial intensity emitted by the X-ray source, and  $I_1(\mathbf{r})$  is the attenuated intensity received by the detector.  $\mathbf{r}(n)$  and  $\mathbf{r}(f)$  are the entry and exit points of the X-ray intersected with the scanning bounding box, where  $n$  and  $f$  indicate the near and far bounds, respectively. After the injection of contrast agent, its concentration within vessels changes over time as it circulates with blood flow, resulting in temporally varying attenuation response  $\mu_2(\mathbf{x}, t)$  in vessel area. And the X-ray attenuation process along the same

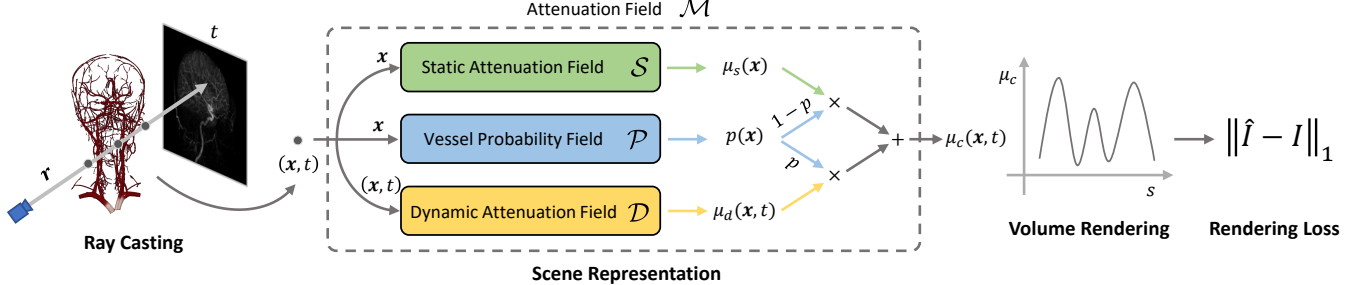


Fig. 3. Overview of our proposed method. We represent the dynamic DSA imaging as a complementary weighted combination of static and dynamic attenuation fields, where the weights assigned to each component are derived from the vessel probability field. Our model is trained by minimizing the disparity between synthesized projections  $\hat{I}$  and real captured DSA images  $I$ .

incident X-ray path transforms from Eq. 1 to the following:

$$I_2(\mathbf{r}, t) = I_1(\mathbf{r}) \exp \left( - \int_{d_1}^{d_2} (\mu_2(\mathbf{r}(s), t) - \mu_1(\mathbf{r}(s))) ds \right) \quad (2)$$

here,  $I_2(\mathbf{r}, t)$  represents the new attenuated intensity received by the detector after injection.  $\mathbf{r}(d_1)$  and  $\mathbf{r}(d_2)$  are the entry and exit points of the X-ray intersected with the vessel, where  $d_1$  and  $d_2$  are the near and far bounds, respectively. Then, we take subtraction between  $I_1(\mathbf{r})$  and  $I_2(\mathbf{r}, t)$  in logarithmic domain to get the intensity  $I(\mathbf{r}, t)$  of DSA image as follows:

$$\begin{aligned} I(\mathbf{r}, t) &= \ln(I_1(\mathbf{r})) - \ln(I_2(\mathbf{r}, t)) \\ &= \int_{d_1}^{d_2} \mu_2(\mathbf{r}(s), t) - \mu_1(\mathbf{r}(s)) ds \\ &= \int_n^f \mu_c(\mathbf{r}(s), t) ds \end{aligned} \quad (3)$$

$\mu_c(\mathbf{x}, t)$  is the attenuation of contrast agent, which is defined as follows:

$$\mu_c(\mathbf{r}(s), t) = \begin{cases} \mu_2(\mathbf{r}(s), t) - \mu_1(\mathbf{r}(s)) & d_1 \leq s \leq d_2 \\ 0 & \text{else} \end{cases} \quad (4)$$

This is what we aim to solve in this study.

### B. Vessel Probability Guided Attenuation Learning

Given a sequence of DSA frame data  $\{\mathbf{I}_i, t_i\}_{i=1}^N$ , our goal is to accurately represent the dynamic imaging process. Here  $N$  stands for the number of training frames and  $i$  denotes the frame index.  $\mathbf{I}_i \in \mathbb{R}^{H \times W}$  refers to the  $i_{th}$  DSA image, and  $t_i$  is the corresponding timestamp. The overview of our framework is depicted in Fig. 3. We aim to learn a 4D mapping function, which we termed as attenuation field  $\mathcal{M}$ , that attempts to map a spatial-temporal coordinate  $(\mathbf{x}, t)$  to the attenuation value  $\mu_c$  of contrast agent, mathematically  $\mathcal{M} : (\mathbf{x}, t) \in \mathbb{R}^3 \times \mathbb{R} \rightarrow \mu_c \in \mathbb{R}_0^+$ .

1) *Naive Solution*: In DSA imaging, the majority of the scanned scene consists of static backgrounds, with only the vessel areas containing the flowing contrast agent. Therefore, a straightforward idea is to decompose  $\mathcal{M}$  into two components: the static attenuation field  $\mathcal{S} : \mathbf{x} \in \mathbb{R}^3 \rightarrow \mu_s \in \mathbb{R}_0^+$  and the dynamic attenuation field  $\mathcal{D} : (\mathbf{x}, t) \in \mathbb{R}^3 \times \mathbb{R} \rightarrow \mu_d \in \mathbb{R}_0^+$ . The former is designed to capture unchanging elements of the

scanned scene, while the latter depicts dynamic aspects. Thus, the attenuation of contrast agent can be expressed as the sum of static and dynamic ones:

$$\mu_c(\mathbf{x}, t) = \mu_s(\mathbf{x}) + \mu_d(\mathbf{x}, t) \quad (5)$$

Each of  $\mathcal{S}$  and  $\mathcal{D}$  is composed of a multi-resolution hash encoder [23]  $\mathbf{h}$  followed by a shallow MLPs  $\phi$ , thus  $\mu_s$  and  $\mu_d$  could be further expressed as:

$$\mu_s(\mathbf{x}) = \phi_s(\mathbf{h}_s(\mathbf{x})), \mu_d(\mathbf{x}, t) = \phi_d(\mathbf{h}_d(\mathbf{x}, t)) \quad (6)$$

$\mathbf{h}_s$  is a 3D hash encoder for representing time-independent attributes while  $\mathbf{h}_d$  is a 4D hash encoder for capturing time-varying features. And then the following MLPs, denoted as  $\phi_s$  and  $\phi_d$ , transform the encoded features into attenuation values, where the output activation function is Rectified Linear Unit (ReLU).

We can derive the gradients of  $\mu_s$  and  $\mu_d$  according to Eq. 5 as follows:

$$\frac{\partial \mu_c}{\partial \mu_s} = \frac{\partial \mu_c}{\partial \mu_d} = 1 \quad (7)$$

where the weights of  $\mu_s$  and  $\mu_d$  to the scene representations  $\mu_c$  are considered equal. However, this straightforward addition leads to poor reconstruction results because the model capacity has not been fully utilized. The majority of DSA imaging is time-invariant, such as static backgrounds, which could be accurately reconstructed by the static attenuation field alone. However, these static points will always modify the parameters of dynamic attenuation field due to the persistent gradients, as indicated by  $\frac{\partial \mu_c}{\partial \mu_d} = 1$ . As a result, the dynamic field cannot accurately capture genuine dynamics. Similarly, the static field will also be diminished by the improper gradients, but not that severe, since dynamic flow is much sparser in the scanned scene. Thus, how to achieve proper gradients, especially that of dynamic field, would be the key point to accurately represent dynamic DSA sequence.

2) *Vessel Probability Field*: To model the dynamic DSA imaging process more effectively, we propose to use a time-agnostic vessel probability field  $\mathcal{P} : \mathbf{x} \in \mathbb{R}^3 \rightarrow p \in [0, 1]$ . Here  $\mathcal{P}$  contains another 3D hash encoder  $\mathbf{h}_p$  and decoding MLPs  $\phi_p$ , where the output activation is Sigmoid function. Thus, vessel probability  $p$  can be further expressed as:

$$p(\mathbf{x}) = \phi_p(\mathbf{h}_p(\mathbf{x})) \quad (8)$$

With the help of vessel probability, the attenuation expression transforms from Eq. 5 to the following:

$$\mu_c(\mathbf{x}, t) = (1 - p(\mathbf{x})) \mu_s(\mathbf{x}) + p(\mathbf{x}) \mu_d(\mathbf{x}, t) \quad (9)$$

Eq. 9 represents  $\mu_c$  as a complementary weighted combination of static attenuation  $\mu_s$  and dynamic one  $\mu_d$ , with the weights determined by the vessel probability. Now the gradients of  $\mu_s$  and  $\mu_d$  change from Eq. 7 to the following:

$$\frac{\partial \mu_c}{\partial \mu_s} = 1 - p, \quad \frac{\partial \mu_c}{\partial \mu_d} = p \quad (10)$$

This design is based on the observation that contrast agents only flow within static vessels during DSA scanning process. A high value of  $p(\mathbf{x})$  indicates vessel presence at that given point  $\mathbf{x}$ , typically associated with dynamic contrast flow, since such flow is restricted to vessel areas. It gives a higher weight to  $\mu_d$  and a lower weight to  $\mu_s$ . As a result, during back-propagation, the loss gradients from point  $\mathbf{x}$  would primarily modify the parameters of dynamic field, leaving the static field unaffected. In this way, dynamic properties will be mainly stored in the dynamic field. Conversely, a low value of  $p$  indicates static backgrounds dominate point  $\mathbf{x}$ , increasing the weight of  $\mu_s$  while lessening that of  $\mu_d$ . The loss gradients would chiefly modify the parameters of static field without disrupting dynamic field, ensuring static properties are mainly stored in the static field. In brief, vessel probability provides proper gradients for both static and dynamic fields adaptive to different scene types. The static backgrounds and dynamic contrast agent flow could be accurately captured by static and dynamic fields respectively, without interference between each other. Functioning as a dynamic mask, vessel probability facilitates a self-supervised static-dynamic decomposition and significantly improves the reconstruction quality. So far, we have solved the issue introduced in Eq. 5.

3) *Model Optimization*: The volumetric rendering, as defined in Eq. 3, is applied to each training ray  $\mathbf{r}$  at corresponding timestamp  $t$ . Our model is trained by minimizing L1 distance between synthesized projections  $\hat{I}(\mathbf{r}, t)$  and the real captured DSA images  $I(\mathbf{r}, t)$ .

$$\hat{I}(\mathbf{r}, t) = \int_n^f \mu_c(\mathbf{r}(s), t) ds, \quad \mathcal{L}_1 = \|\hat{I}(\mathbf{r}, t) - I(\mathbf{r}, t)\|_1 \quad (11)$$

Furthermore, the vessel probability field is inherently under-constrained. Given that vessel areas are sparse in DSA imaging scenes, we aim to drive the vessel probability generally towards zero, appearing only in necessary locations. Thus, we introduce another regularization term to reduce noisy artifacts of vessel probability:

$$\mathcal{L}_{reg} = \|p(\mathbf{x})\|_1 \quad (12)$$

$\mathbf{x}$  is random sample point within the scanning bounding box. Our overall loss is a weighted summation of  $\mathcal{L}_1$  and  $\mathcal{L}_{reg}$ :

$$\mathcal{L} = \mathcal{L}_1 + \lambda_{reg} \mathcal{L}_{reg} \quad (13)$$

where  $\lambda_{reg}$  is a weighting factor used to adjust the influence of the regularization term.

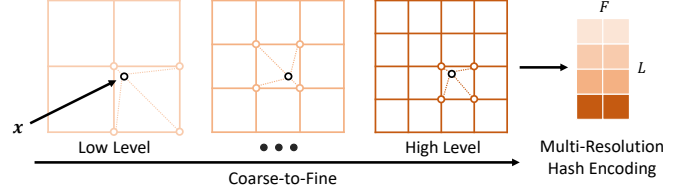


Fig. 4. 2D toy example of coarse-to-fine progressive training with multi-resolution hash encoding. We gradually activate different levels of hash grids from coarse to fine to mitigate noisy artifacts caused by high-frequency overfitting.

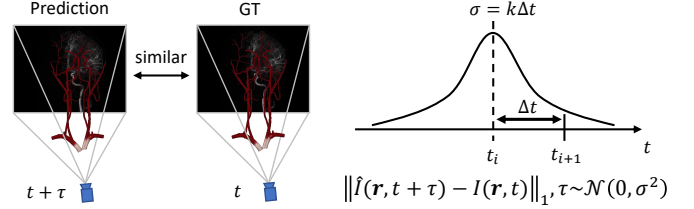


Fig. 5. Illustration of temporal perturbed rendering loss. Projection value should be quite similar at slightly perturbed timestamps from the same viewpoint. The temporal perturbation is simply modeled as a Gaussian noise.

### C. Training Strategies

1) *Coarse-to-Fine Progressive Training*: As illustrated in Sec. III-B, we apply multi-resolution hash encoder as our encoding module following Instant-NGP [23]. The hash encoder utilizes multi-resolution voxel grids to represent the reconstructed scene, where each grid cell is mapped to a hash entry with trainable feature vectors by hash function. A 2D toy example is illustrated in Fig. 4. Given a 2D query coordinate  $\mathbf{x} \in \mathbb{R}^2$ , it first acquires hash encoding  $\mathbf{h}^l(\mathbf{x}) \in \mathbb{R}^F$  at each level by interpolating the surrounding grid cell feature vectors at that level, where  $F$  is the dimension of feature vector. Then the queried features across all  $L$  levels are concatenated together to form multi-resolution hash encoding  $\mathbf{h}(\mathbf{x}) = \{\mathbf{h}^l(\mathbf{x})\}_{l=1}^L \in \mathbb{R}^{LF}$ :

Different resolutions of hash grids capture different levels of details of the scene. High-resolution hash grids typically capture high-frequency components, while low-resolution ones represent low-frequency elements. However, enabling all hash grids from the start of training can easily lead to overfitting on high-frequency components, hindering the model from exploring low-frequency information and causing undesired noisy artifacts [26]. To mitigate such high-frequency overfitting issue, we adopt a progressive training strategy [26], [28], [29] that gradually unmasks different levels of hash grids, from coarse to fine. Initially, the model is trained using only a few low-resolution hash grids, while the finer levels are inactive. As training progresses, finer hash grids are sequentially activated, according to a predefined schedule of iterations. This approach effectively reduces high-frequency noise, contributing to better vascular geometries with smoother surfaces.

2) *Temporal Perturbed Rendering Loss*: Given a sparse set of dynamic DSA images as training set, the model tends to overfit to the training frames without any temporal

regularization, resulting in discontinuities and artifacts when observed at testing frames. A crucial insight is that blood flow is temporally continuous, and the flow states between neighboring timestamps are expected to be quite similar. Therefore, when observing from the same viewpoint, the projection value should remain stable at slightly perturbed timestamps. Based on this observation, we propose to use a temporal perturbed rendering loss to enforce our model to be temporally consistent. The rendering loss transforms from Eq. 11 to the following:

$$\mathcal{L}_1 = \left\| \hat{I}(\mathbf{r}, t + \tau) - I(\mathbf{r}, t) \right\|_1, \quad \tau \sim \mathcal{N}(0, \sigma^2) \quad (14)$$

Eq. 14 could be better illustrated with the aid of Fig. 5. The interval between neighboring training timestamps is denoted as  $\Delta t = t_{i+1} - t_i$ . Temporal perturbation is simply modeled as a Gaussian noise,  $\tau \sim \mathcal{N}(0, \sigma^2)$ , where  $\sigma$  is the standard deviation that controls the perturbation range. We set  $\sigma = k\Delta t$ , with  $k$  denoting the Gaussian kernel size. This technique provides temporal augmentation in the training phase by connecting neighboring timestamps, thus improving generalization ability when observed from the testing frames.

#### D. Vascular Reconstruction

Once the model is well-trained, we could reconstruct volumetric contrast agent image at any timestamp  $t$  by inferring the model at the predefined spatial coordinates. That is,  $V_c(t) : \{\mathbf{x}_j, \mu_c(\mathbf{x}_j, t)\}_{j=1}^{|\mathbf{X}|}$ , where  $\mathbf{X}$  represents the set of predefined spatial coordinates,  $|\mathbf{X}|$  denotes its length, and  $j$  is the spatial coordinate index. Moreover, due to the continuous contrast agent flow, the information of  $V_c(t)$  is always changing. To obtain a comprehensive reconstruction of the vascular structures, we opt to average  $V_c(t)$  across all the training timestamps as our reconstructed vascular result, *i.e.*,  $\bar{V}_c = \frac{1}{N} \sum_{i=1}^N V_c(t_i)$ . We could also derived various volumetric images from our model following a similar way: vessel probability volume  $V_p : \{\mathbf{x}_j, p(\mathbf{x}_j)\}_{j=1}^{|\mathbf{X}|}$ , static attenuation volume  $V_s : \{\mathbf{x}_j, \mu_s(\mathbf{x}_j)\}_{j=1}^{|\mathbf{X}|}$ , dynamic attenuation volume  $V_d(t) : \{\mathbf{x}_j, \mu_d(\mathbf{x}_j, t)\}_{j=1}^{|\mathbf{X}|}$ , and averaged dynamic attenuation volume  $\bar{V}_d = \frac{1}{N} \sum_{i=1}^N V_d(t_i)$ .  $V_p$  could be utilized to selectively mask out the static component volume as  $(1 - V_p)V_s$ , the dynamic component volume as  $V_p V_d(t)$  and the averaged dynamic component volume as  $V_p \bar{V}_d$  for further analysis. Here,  $\mathbf{1}$  represents a matrix consisting entirely of ones. For more details and visualization, please refer to Sec. IV-B.

## IV. EXPERIMENT

### A. Experimental Settings

1) *Dataset*: In this study, we primarily utilized datasets collected from 15 different patients at Wuhan Union Hospital. For each patient, the DSA scanning system recorded two sets of X-ray images, *i.e.*, the mask run and the fill run. Each set comprises of 133 frames, taken at uniform angular increments within a range of 198 degrees. Additionally, the system employed the FDK algorithm to reconstruct vascular results using these two sets of X-ray images. Each reconstructed

volume has a resolution of  $512 \times 512 \times 395$  and an isotropic voxel size of 0.4881mm except for case #7 and #13. For case #7 and #13, each of their reconstructed volume has a resolution of  $512 \times 512 \times 506$  with an isotropic voxel size of 0.3802mm. However, these reconstruction results are not entirely accurate and are primarily used as reference for evaluating the 3D vessel reconstruction task. DSA sequence was derived following the subtraction process as described in Sec. III-A. From these DSA images, subsets of 30 views, 40 views, 50 views, and 60 views at uniformly spaced angles were selected for training purpose, while the rest were reserved as testing set to assess the quality of 2D view synthesis. Each projection has a resolution of  $1240 \times 960$  with a pixel size of  $0.3219\text{mm} \times 0.3208\text{mm}$ . As for case #7 and case #13, the projection resolution is  $960 \times 960$  and the pixel size is  $0.3239\text{mm} \times 0.3201\text{mm}$ . The Source-to-Object distance is 750mm and Source-to-Detector distance is 1200mm. The rotation angle for each projection is also recorded in the DICOM file.

2) *Implementation Details*: Our proposed method includes three implicit fields, each comprising a hash encoder followed by three-layer MLPs with a hidden size of 128. The hash encoders  $\mathbf{h}_s$  and  $\mathbf{h}_p$  are configured with identical hyper-parameters. Both of them consist of 12 hash levels, each level containing a maximum of  $2^{19}$  entries, with every entry being an 8-dimensional learnable feature vector. Their base resolution is set to 8, with a scaling factor of 1.45. The initial activating level is 4, with subsequent levels activated every 2500 iterations. The encoder  $\mathbf{h}_d$  shares almost the same hyper-parameters as other two encoders, but with two changes of its base resolution 2 and the scaling factor 1.4, to better suit the smaller temporal resolution compared to spatial resolution in our dataset. For more details about hash encoder and these hyper-parameters, please refer to Instant-NGP [23]. We set the regularization weight  $\lambda_{reg}$  to 0.01, the Gaussian kernel size  $k$  to 1, the random ray batch size to 2048, and the regularization points size to 10k. The Adam optimizer is employed for optimization, starting with an initial learning rate of  $7.5 \times 10^{-4}$ , which decays by a factor of 0.9 every 5k iterations. We train our model for a total of 100k iterations. All experiments are conducted on a single A100 GPU.

3) *Competing Methods and Evaluation Metrics*: We compare our method with the traditional FDK method, and NeRF-based methods, including NAF, and TiAVox. Due to the proprietary nature of commercial DSA systems, our reconstructions are limited to using only the basic version of the FDK algorithm. Our evaluation primarily focuses on 3D vessel reconstruction, while 2D view synthesis is considered as a secondary focus. For 3D vessel reconstruction, the reconstructed results from the DSA scanning system serve as our reference standard, which will be compared with the outcomes from those competing methods mentioned above. We first convert these reconstructed results into mesh format using marching cubes algorithm [39]. The accuracy of the meshes from these algorithms, compared to the reference one, is assessed using two metrics: Chamfer Distance (CD) and the Hausdorff Distance (HD), both quantified in millimeters. Typically, lower CD and HD values indicate better 3D reconstruction accuracy.

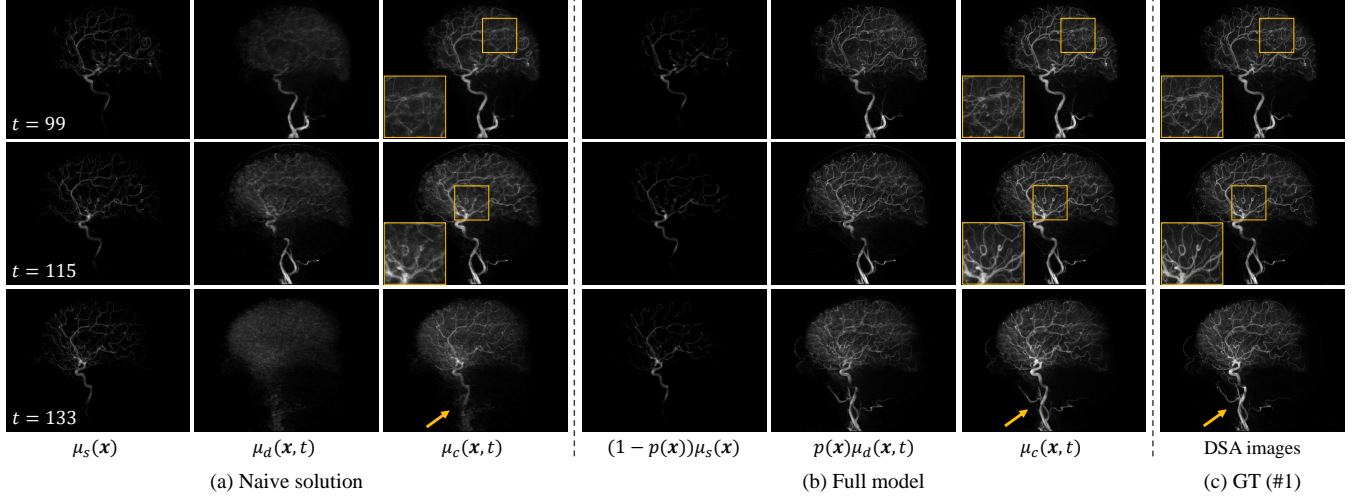


Fig. 6. Visualization of 2D view synthesis. (a) Naive solution: rendering of static attenuation  $\mu_s(\mathbf{x})$ , dynamic attenuation  $\mu_d(\mathbf{x}, t)$ , and contrast agent attenuation  $\mu_c(\mathbf{x}, t)$ . (b) Full model: rendering of static component  $(1 - p(\mathbf{x}))\mu_s(\mathbf{x})$ , dynamic component  $p(\mathbf{x})\mu_d(\mathbf{x}, t)$ , and contrast agent attenuation  $\mu_c(\mathbf{x}, t)$ . (c) Ground truth of DSA images.

As a supplementary evaluation, 2D view synthesis is assessed by examining the synthesized projection quality of the testing frames. This is achieved by measuring the Peak Signal-to-Noise Ratio (PSNR) and the Structural Similarity Index (SSIM) [40] metrics, where higher PSNR and SSIM values signify better quality in 2D view synthesis.

### B. Model Output Analysis

Given the complexity of our model outputs, especially the dynamic aspects, we aim to provide a comprehensive illustration through both 3D visualizations and 2D renderings in this section. All results presented here were derived from case #1 in our dataset, with 40 training views.

**1) 3D Vessel Reconstruction:** As mentioned in Sec. III-D, we could derive various volumetric images by inferring our trained model at predefined spatial coordinates within the scanning bounding box. These images maintain the same resolution and spacing as the reference reconstructed image provided by the DSA system.

Fig. 7(b)(10) displays  $V_p$ , which closely resembles the vascular structure, indicating our vessel probability field's ability to capture meaningful vascular patterns. Fig. 7(b)(5) depicts  $(1 - V_p)V_s$ , showing the static components of contrast agent flow shared across different timestamps. The dynamic elements of contrast flow are provided in Fig. 7(b)(1-3), which present a series of  $V_pV_d(t)$  across several training timestamps. Fig. 7(b)(6-8) show a series of contrast flow  $V_c(t)$ , which could be obtained by combining the statics and dynamics. These results demonstrate our model's capability in effectively separating static and dynamic aspects under the guidance of vessel probability. Finally, Fig. 7(b)(4,9) showcase  $V_p\bar{V}_d$  and  $\bar{V}_c$ . Notably,  $\bar{V}_c$  serves as the final output of our model, representing the reconstructed vascular structure. For comparison, Fig. 7(a)(10) presents the reference reconstructed result provided by DSA system. In this case, the CD value is 1.09mm, and HD value is 1.83mm.  $\bar{V}_c$  closely matches the

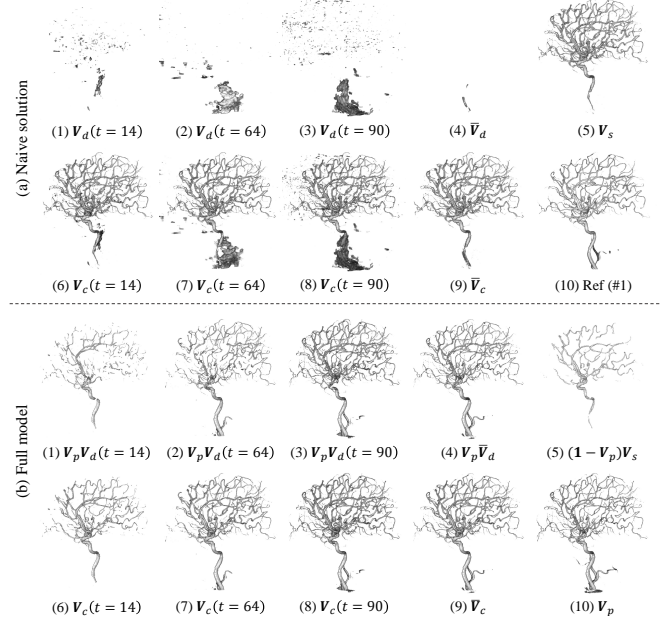


Fig. 7. Visualization of 3D vessel reconstruction. (a) Naive solution: (1-3) dynamic attenuation volume  $V_d(t)$ , (4) averaged dynamic attenuation volume  $\bar{V}_d$ , (5) static attenuation volume  $V_s$ , (6-8) contrast agent volume  $V_c(t)$ , (9) reconstructed vascular structure  $\bar{V}_c$ , and (10) reference vascular structure. (b) Full model: (1-3) dynamic component volume  $V_pV_d(t)$ , (4) averaged dynamic component volume  $V_p\bar{V}_d$ , (5) static component volume  $(1 - V_p)V_s$ , (6-8) contrast agent volume  $V_c(t)$ , (9) reconstructed vascular structure  $V_c$ , and (10) vessel probability volume  $V_p$ .

reference structure, achieved with less than one-third of the input views, highlighting the effectiveness of our model.

We also provide the reconstruction results from the naive solution which is devoid of vessel probability field as discussed in Sec. III-B1 to validate its efficacy. Fig. 7(a)(4,5,9) showcases  $\bar{V}_d$ ,  $V_s$ , and  $\bar{V}_c$ . Fig. 7(a)(1-3) and Fig. 7(a)(6-8) display series of  $V_d(t)$  and  $V_c(t)$ . Notably,  $V_d(t)$  and  $\bar{V}_d$  appear noisy without any discernible vessel structures, indicating the chal-

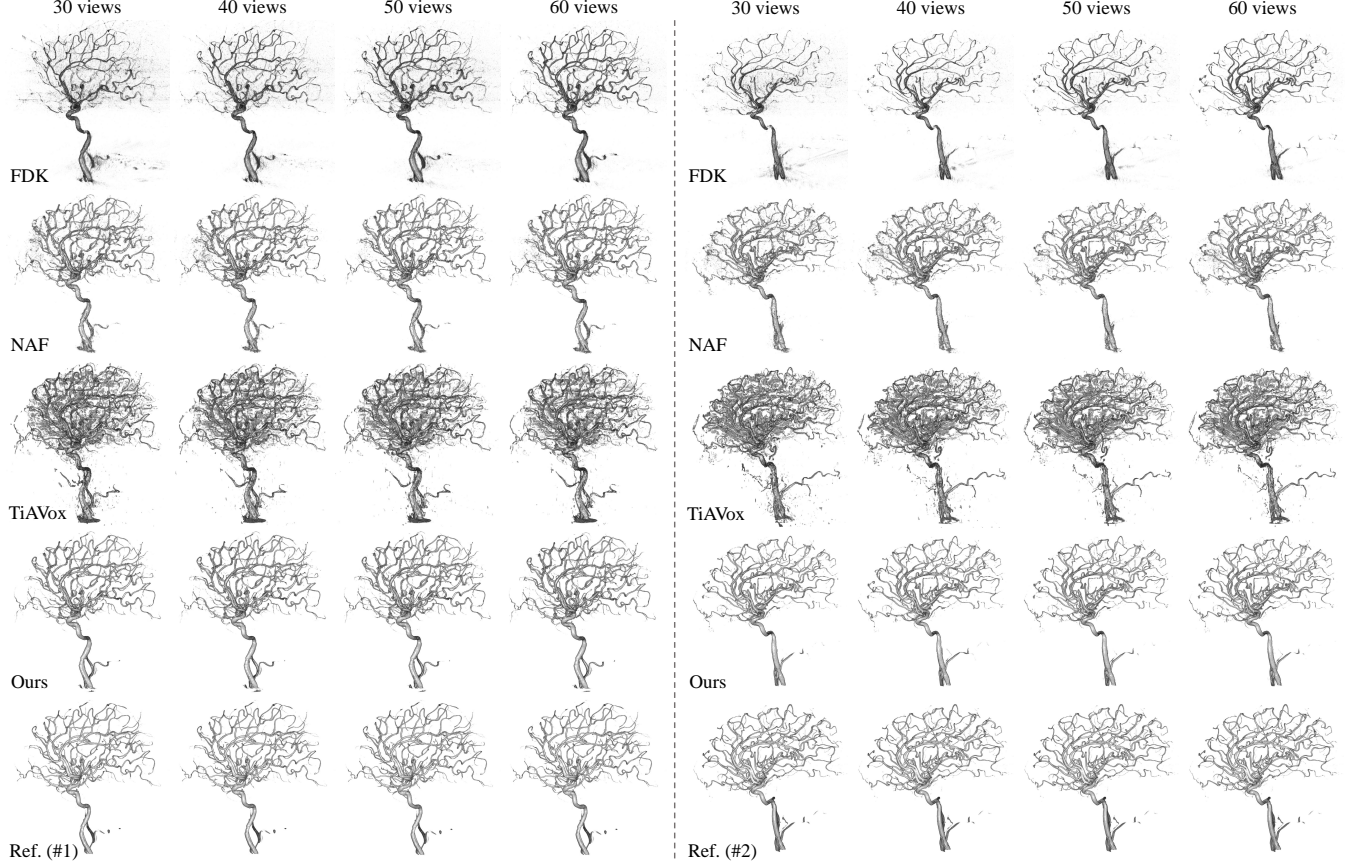


Fig. 8. Qualitative comparison on 3D vessel reconstruction. Our method significantly outperforms all the other methods and produces reliable reconstruction quality, even with only 30 input views.

TABLE I  
QUANTITATIVE COMPARISON ON 3D VESSEL RECONSTRUCTION. THE BEST-PERFORMING METHOD IS SHOWN IN BOLD.

Method	30 views		40 views		50 views		60 views	
	CD (mm) ↓	HD (mm) ↓						
FDK	4.82±1.73	14.45±5.98	3.35±0.76	10.29±3.42	3.08±0.73	8.80±2.28	2.47±0.58	7.09±2.28
NAF	2.72±0.68	6.66±2.00	2.32±0.49	6.05±2.76	2.14±0.45	5.98±2.90	1.98±0.37	5.55±2.70
TiAVox	2.37±0.27	6.09±0.99	2.42±0.24	6.07±0.91	2.32±0.19	5.86±0.96	2.31±0.24	5.99±1.27
Ours	<b>1.46±0.20</b>	<b>2.95±0.85</b>	<b>1.40±0.20</b>	<b>2.54±0.57</b>	<b>1.35±0.19</b>	<b>2.43±0.63</b>	<b>1.29±0.17</b>	<b>2.25±0.47</b>

lengh in achieving a clear decomposition between statics and dynamics without the vessel probability field. Additionally, the quality of both  $V_c(t)$  and  $\bar{V}_c$  is substantially degraded. The CD and HD values deteriorate to 2.48mm and 12.51mm, respectively. These results emphasize the vital importance of the vessel probability field in ensuring clear static-dynamic decomposition and the quality of the reconstructed vascular structure.

2) *2D View Synthesis*: Furthermore, our model can be used to synthesize 2D projections of contrast agent  $\mu_c(\mathbf{x}, t)$  following Eq. 11 given any desired viewpoints with timestamps. By altering the integral variable, we can similarly render  $(1 - p(\mathbf{x}))\mu_s(\mathbf{x})$  and  $p(\mathbf{x})\mu_d(\mathbf{x}, t)$ , which corresponds to the static and dynamic components of  $\mu_c(\mathbf{x}, t)$ , respectively. Fig. 6(b) presents a subset of these renderings from the

testing frames. These images clearly demonstrate that our model not only achieves a clear separation between static and dynamic components but also provides high-quality novel view synthesis, as evident when compared to the ground truth shown in Fig. 6(c). In this case, the PSNR and SSIM metrics averaged over the testing set are 33.41dB and 0.811, respectively.

In contrast, when we apply the naive solution to render  $\mu_s(\mathbf{x})$ ,  $\mu_d(\mathbf{x}, t)$ , and  $\mu_c(\mathbf{x}, t)$  as depicted in Fig. 6(a), the results are significantly different. The decomposition between static and dynamic components appears ambiguous, resulting in inferior synthesized DSA images characterized by blurring and loss of details. The PSNR and SSIM metrics degrade to 30.29dB and 0.777, respectively. This further demonstrates the effectiveness of our proposed vessel probability field.

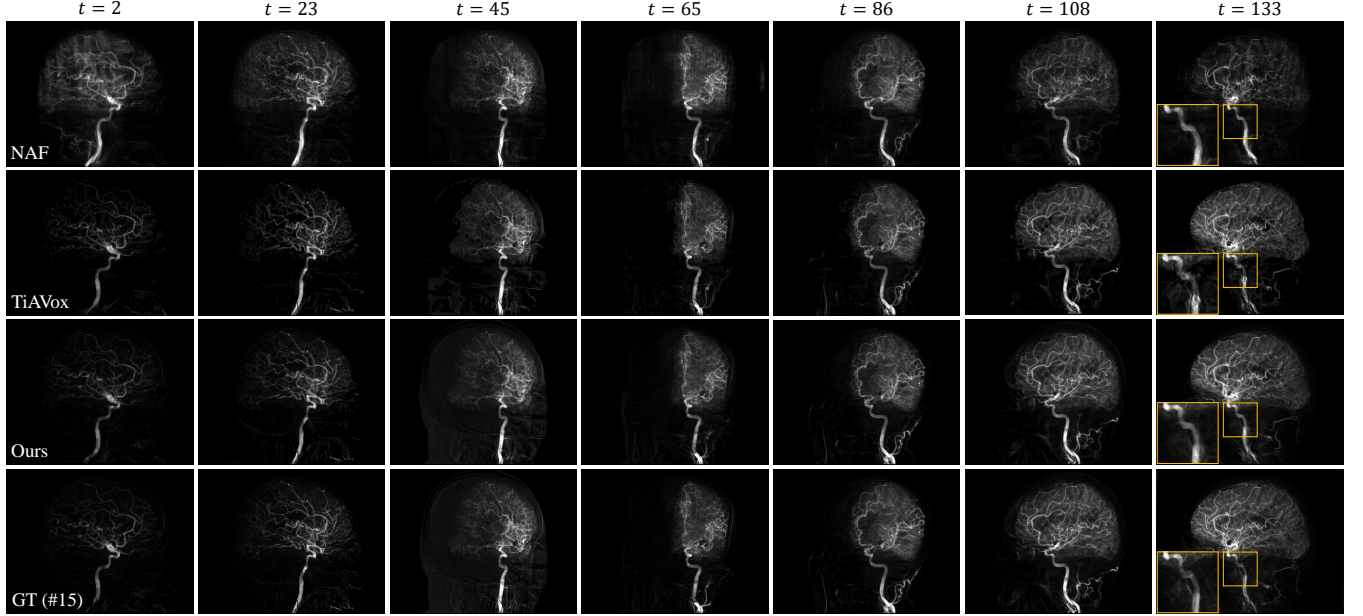


Fig. 9. Qualitative comparison on 2D view synthesis. Our method could effectively model the dynamic DSA imaging process, yielding better 2D view synthesis quality.

TABLE II  
QUANTITATIVE COMPARISON ON 2D VIEW SYNTHESIS. THE BEST-PERFORMING METHOD IS SHOWN IN BOLD.

Method	30 views		40 views		50 views		60 views	
	PSNR (dB) $\uparrow$	SSIM $\uparrow$						
NAF	28.37 $\pm$ 0.98	0.741 $\pm$ 0.043	28.53 $\pm$ 0.97	0.750 $\pm$ 0.042	28.73 $\pm$ 1.02	0.757 $\pm$ 0.041	28.80 $\pm$ 1.00	0.760 $\pm$ 0.038
TiAVox	32.24 $\pm$ 1.27	0.729 $\pm$ 0.045	32.70 $\pm$ 1.33	0.735 $\pm$ 0.044	32.96 $\pm$ 1.34	0.738 $\pm$ 0.044	33.07 $\pm$ 1.29	0.739 $\pm$ 0.042
Ours	<b>33.71<math>\pm</math>1.38</b>	<b>0.825<math>\pm</math>0.031</b>	<b>34.43<math>\pm</math>1.35</b>	<b>0.833<math>\pm</math>0.029</b>	<b>34.95<math>\pm</math>1.40</b>	<b>0.839<math>\pm</math>0.028</b>	<b>35.28<math>\pm</math>1.37</b>	<b>0.842<math>\pm</math>0.025</b>

### C. Experimental Results

1) *3D Vessel Reconstruction*: Fig. 8 presents a qualitative comparison on 3D vessel reconstruction from cases #1 and case #2 in our dataset. The traditional FDK algorithm displays poor reconstruction quality with a significant loss of details as it fails to account for temporal aspects in dynamic DSA sequences. The outputs are noticeable with streaky artifacts and noises due to sparse input, especially for 30 views. NAF provides better vascular structures than FDK with a powerful NeRF-based optimization framework. However, it also neglects the temporal dimension. This omission results in the loss of details and leads to considerable noise in the reconstructions. TiAVox considers the temporal aspect using a learnable 4D voxel grid, but fails to capture the inter-frame relationships within DSA sequences, leading to severe model capacity waste caused by redundant static points storage. Moreover, the memory overhead restricts spatial and temporal resolution to  $320^3$  and 7, respectively. These factors cause blurry reconstructions with significant noises and artifacts. Note that the reconstructed result of TiAVox is also obtained by averaging  $V(t)$  across all training timestamps. In contrast, our algorithm demonstrates excellent reconstruction quality, even with only 30 input views. It delivers smooth surfaces with reduced noise, and the vessel details are rich, closely

matching with the reference images. This success highlights our approach’s effectiveness in reconstructing vascular structures from sparse-view dynamic DSA images.

Table I further provides quantitative comparison of different methods with CD and HD metrics. The trends observed in this table closely aligns with those qualitative results. FDK consistently exhibits the poorest CD and HD values across all view counts, reflecting its limitation in handling sparse data and temporal aspects. Both NAF and TiAVox show improved metrics but have their own limitations: NAF lacks dynamic modeling, while TiAVox struggles with inefficient dynamic modeling. Across various view counts, our approach outperforms all other methods in terms of both CD and HD metrics. It underscores our superior ability in reconstructing 3D vascular structures with sparse and dynamic DSA inputs.

2) *2D View Synthesis*: Fig. 9 demonstrates a qualitative comparison on 2D view synthesis across a series of testing timestamps. The results were derived from case #15 in our dataset, with 40 training views. It should be noted that FDK cannot synthesize 2D projections, so it is absent in this comparison. The NAF approach falls short in synthesizing dynamic DSA sequence due to its disregard for the temporal dimension, leading to static projections with unsatisfied quality. On the other hand, TiAVox, leveraging a learnable 4D voxel grid, successfully creates dynamic sequence and demonstrates

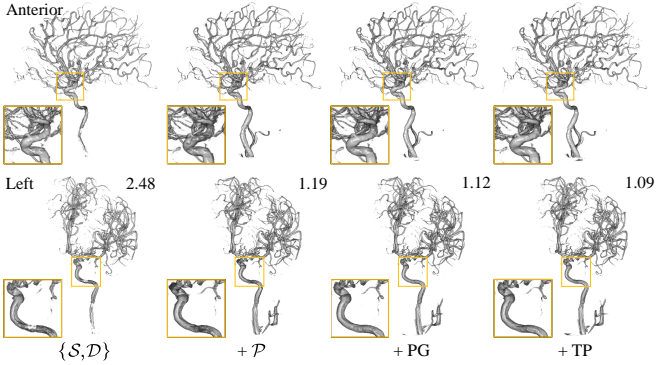


Fig. 10. Qualitative results of 3D vessel reconstruction for ablation study on different components. CD (mm) values are provided for comparison.

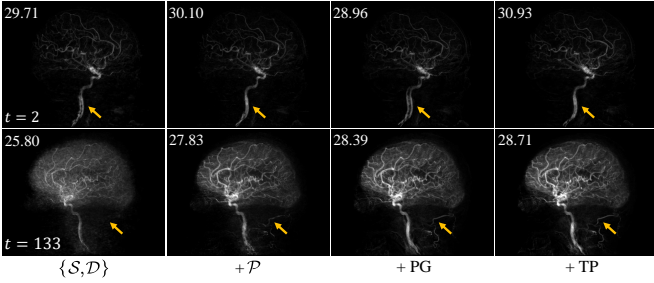


Fig. 11. Qualitative results of 2D view synthesis for ablation study on different components. PSNR (dB) values are provided for comparison.

results comparable to ours. Nevertheless, its shortcomings in addressing inter-frame relationships and limited spatio-temporal resolution result in inferior quality compared to our approach. This is particularly evident with noisy artifacts as highlighted in the yellow box at  $t = 133$ . Our method effectively models dynamic DSA sequence, surpassing all these limitations, thereby offers impressive quality in 2D view synthesis.

Table II delivers a quantitative comparison among competing methods on PSNR and SSIM metrics. We notice similar trends to those in the qualitative results. NAF consistently exhibits lowest scores in both metrics. While TiAVox shows considerable improvement, it is still inferior to our method. These results confirm our superiority in 2D view synthesis, especially notable at higher view counts.

#### D. Ablation Study

1) *Ablation Study on Model Components:* We first conduct ablation studies to verify the effectiveness of different model components, including the vessel probability field and training strategies that we proposed one by one. All results provided in this section were derived with 40 training views.

Table III presents the quantitative results.  $\{\mathcal{S}, \mathcal{D}\}$  denotes the naive solution as discussed in Sec. III-B1, which only uses static and dynamic attenuation field to interpret the dynamic scanning scene.  $\mathcal{P}$  represents vessel probability field, while PG and TP stand for coarse-to-fine progressive training and temporal perturbed rendering loss, respectively. Each ticked  $\checkmark$  sample indicates the inclusion of the specific component.

TABLE III  
QUANTITATIVE RESULTS FOR ABLATION STUDY ON DIFFERENT COMPONENTS.

$\{\mathcal{S}, \mathcal{D}\}$	$\mathcal{P}$	PG	TP	CD (mm) $\downarrow$	HD (mm) $\downarrow$	PSNR (dB) $\uparrow$	SSIM $\uparrow$
$\checkmark$				3.10 $\pm$ 1.44	9.84 $\pm$ 5.46	30.60 $\pm$ 1.20	0.786 $\pm$ 0.034
$\checkmark$	$\checkmark$			1.50 $\pm$ 0.20	3.18 $\pm$ 1.03	34.08 $\pm$ 1.42	0.823 $\pm$ 0.032
$\checkmark$	$\checkmark$	$\checkmark$		1.42 $\pm$ 0.19	2.75 $\pm$ 0.64	34.26 $\pm$ 1.46	0.828 $\pm$ 0.030
$\checkmark$	$\checkmark$	$\checkmark$	$\checkmark$	1.40 $\pm$ 0.20	2.54 $\pm$ 0.57	34.43 $\pm$ 1.35	0.833 $\pm$ 0.029

The naive solution yields the least effective results in both 3D vessel reconstruction and 2D view synthesis, as evidenced by the lowest performance across all metrics. The involvement of the vessel probability field significantly improves performance in all metrics. This underscores the crucial role of vessel probability field which has already been revealed in Sec. IV-B. The incorporation of PG and TP further boosts our results, confirming the effectiveness of these two training strategies.

Fig. 10 and Fig. 11 display the qualitative results of 3D vessel reconstruction and 2D view synthesis across various settings. In Fig. 10, we present both anterior and left side views of reconstructed vessels along with CD values from case #1. Notably, the incorporation of vessel probability field leads to a more complete vessel structure with much lower CD value. However, it also introduces surface noises, as highlighted in the yellow box. With the addition of progressive training, there is a significant reduction in these noisy artifacts, resulting in a smoother surface and improved geometry accuracy. This improvement demonstrates that progressive training effectively assists the model in capturing low-frequency structures while filtering out high-frequency noises. In Fig. 11, we present the synthesized projections at two testing timestamps, e.g.,  $t = 2$  and 133, along with PSNR values from case #15. Overall, as each component is included, the synthesized projections become more complete and sharper. However, the introduction of progressive training sometimes lead to discontinuous ghosting artifacts in the testing frames, as indicated by the yellow arrow at  $t = 2$ . This is because progressive training prioritizes optimizing low-frequency components over high-frequency ones, inevitably compromising the model's capacity to capture rapid changes during initial frames when cervical artery emerge swiftly. Thus it tends to overfit to training frames, resulting in artifacts in the testing ones. Notably, the inclusion of temporal perturbation significantly reduces those discontinuous artifacts. It mitigates training overfitting by connecting neighboring timestamps, encouraging our model to be temporally consistent, thereby enhancing the quality of synthesized projections.

2) *Ablation Study on Regularization Term:* Next, we study the impact of the regularization term,  $L_{reg}$ , on our model's performance under 40 training views, while keeping all the other model components enabled.

Table IV reveals that omitting the regularization term diminishes model performance across all evaluated metrics. We present a 3D visual example from case #2. As presented in Fig. 12, the absence of the regularization term results in significant noise in the vessel probability image, impairing the

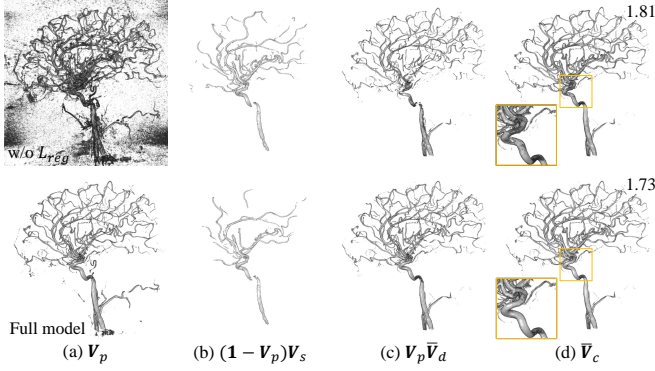


Fig. 12. Qualitative results of 3D vessel reconstruction for ablation study on regularization term. (a) Vessel probability volume  $V_p$ . (b) Static component volume  $(1 - V_p)V_s$ . (c) Averaged dynamic component volume  $V_p\bar{V}_d$ . (d) Reconstructed vessel structure  $\bar{V}_c$ . CD (mm) values are provided for comparison.

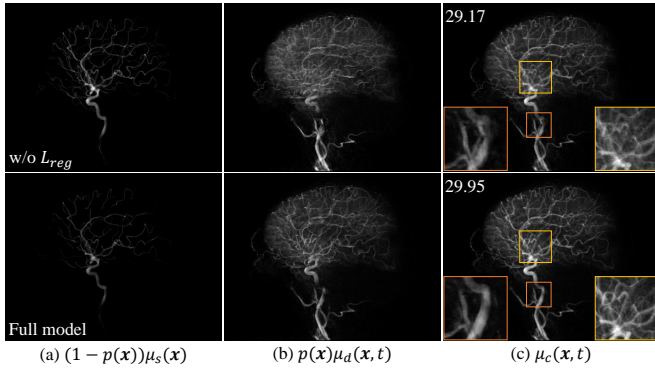


Fig. 13. Qualitative results of 2D view synthesis for ablation study on regularization term. Rendering of (a) static attenuation  $(1 - p(\mathbf{x}))\mu_s(\mathbf{x})$ , (b) dynamic attenuation  $p(\mathbf{x})\mu_d(\mathbf{x}, t)$ , and (c) contrast agent attenuation  $\mu_c(\mathbf{x}, t)$  at timestamp  $t = 133$ . PSNR (dB) values are provided for comparison.

model's capacity to distinguish between statics and dynamics. This leads to noticeable surface noises as highlighted in the yellow box, with a decrease in geometry accuracy as indicated by the CD values. Additionally, Fig. 13 shows 2D renderings at test timestamp  $t = 133$  from case #1. Similarly, the lack of the regularization term hinders the model to achieve clear static-dynamic decomposition, resulting in a degradation of the synthesized projections quality as signified by the PSNR values. This decline is marked by floating artifacts (orange box), along with blurring and loss of details (yellow box).

3) *Ablation Study on Gaussian Kernel Size*: At last, we study the impact of Gaussian kernel size  $k$  on 2D view synthesis under 40 training views. Intuitively, both excessively large and small values of  $k$  could be detrimental. When  $k$  is too small, the temporal perturbation becomes ineffective. And conversely, when  $k$  is too large, it tends to connect timestamps that are too far apart, thereby impairing the rendering quality. To investigate this, we test the quality of synthesized projections under five different settings of  $k$  values: 0, 0.5, 1, 2, and 3, as detailed in Table V. According to this table,  $k = 1$  achieves the best performance in terms of both PSNR and SSIM metrics. Consequently, we choose  $k = 1$  in our experiments.

TABLE IV  
QUANTITATIVE RESULTS FOR ABLATION STUDY ON REGULARIZATION TERM.

	CD (mm) ↓	HD (mm) ↓	PSNR (dB) ↑	SSIM ↑
w/o $L_{reg}$	$1.53 \pm 0.24$	$3.62 \pm 1.38$	$34.03 \pm 1.47$	$0.826 \pm 0.031$
Full model	$1.40 \pm 0.20$	$2.54 \pm 0.57$	$34.43 \pm 1.35$	$0.833 \pm 0.029$

TABLE V  
QUANTITATIVE RESULTS FOR ABLATION STUDY ON GAUSSIAN KERNEL SIZE. PSNR IS QUANTIFIED IN dB.

	0	0.5	1	2	3
PSNR ↑	$34.26 \pm 1.46$	$34.40 \pm 1.39$	$34.43 \pm 1.35$	$34.33 \pm 1.36$	$34.17 \pm 1.36$
SSIM ↑	$0.828 \pm 0.030$	$0.831 \pm 0.029$	$0.833 \pm 0.029$	$0.833 \pm 0.029$	$0.832 \pm 0.030$

## V. DISCUSSION

In summary, we successfully address sparse-view dynamic DSA reconstruction problem. Our method leverages a time-agnostic vessel probability field to guide the attenuation learning process effectively. And we further incorporate two training strategies to improve our model performance: coarse-to-fine progressive training and temporal perturbed rendering loss. These two strategies have been proved to enhance the vascular geometry accuracy and enforce temporal consistency, respectively. Our model demonstrates impressive performance, achieving a CD of 1.46mm in 3D vessel reconstruction and a PSNR of 33.71dB in 2D view synthesis, with only 30 input views. This is merely 22.56% of typical clinical collection of 133 views, thereby substantially reducing radiation exposure.

However, our model still has some limitations. One significant drawback is the time inefficiency. Our algorithm takes around two hours to finish training and reconstruction for each case, which is much slower compared to the few seconds needed by the FDK algorithm in commercial DSA system. This limitation poses a challenge for practical application in the real-world clinical settings. Additionally, there is no standardized procedure for merging the reconstruction results from different timestamps. Currently, we simply average them to obtain our final reconstructed vessel structures, which yields satisfactory results. However, there may be a more appropriate weighting mechanism with further exploration. We leave these aspects as our future work.

## VI. CONCLUSION

In this study, we have developed a comprehensive method designed to reconstruct 3D vessel structures from sparse-view 2D dynamic DSA images. Our method introduces a time-agnostic vessel probability field to model dynamic DSA imaging process effectively, which is inspired by the fact that the vessels remain static during the scanning process. We further employ two training strategies to improve our reconstruction quality, *i.e.*, coarse-to-fine progressive training and temporal perturbed rendering loss. Extensive experiments have demonstrated promising results in both 3D vessel reconstruction and 2D view synthesis. We will further improve our

algorithm to address above mentioned limitations particularly on time inefficiency in the future.

## REFERENCES

- [1] K. Ruedinger, S. Schafer, M. Speidel, and C. Strother, “4d-dsa: development and current neurovascular applications,” *American Journal of Neuroradiology*, vol. 42, no. 2, pp. 214–220, 2021.
- [2] C. Sandoval-Garcia, K. Royalty, P. Yang, D. Niemann, A. Ahmed, B. Aagaard-Kienitz, M. K. Başkaya, S. Schafer, and C. Strother, “4d dsa a new technique for arteriovenous malformation evaluation: a feasibility study,” *Journal of neurointerventional surgery*, 2015.
- [3] S. Lang, P. Göllitz, T. Strüffert, J. Rösch, K. Rössler, M. Kowarschik, C. Strother, and A. Doerfler, “4d dsa for dynamic visualization of cerebral vasculature: a single-center experience in 26 cases,” *American Journal of Neuroradiology*, vol. 38, no. 6, pp. 1169–1176, 2017.
- [4] C. Sandoval-Garcia, K. Royalty, B. Aagaard-Kienitz, S. Schafer, P. Yang, and C. Strother, “A comparison of 4d dsa with 2d and 3d dsa in the analysis of normal vascular structures in a canine model,” *American Journal of Neuroradiology*, vol. 36, no. 10, pp. 1959–1963, 2015.
- [5] L. A. Feldkamp, L. C. Davis, and J. W. Kress, “Practical cone-beam algorithm,” *Josa a*, vol. 1, no. 6, pp. 612–619, 1984.
- [6] R. Fahrig, A. Fox, S. Lownie, and D. Holdsworth, “Use of a c-arm system to generate true three-dimensional computed rotational angiograms: preliminary in vitro and in vivo results.,” *American journal of neuroradiology*, vol. 18, no. 8, pp. 1507–1514, 1997.
- [7] L. Shen, W. Zhao, and L. Xing, “Patient-specific reconstruction of volumetric computed tomography images from a single projection view via deep learning,” *Nature biomedical engineering*, vol. 3, no. 11, pp. 880–888, 2019.
- [8] Y. Kasten, D. Doktovsky, and I. Kovler, “End-to-end convolutional neural network for 3d reconstruction of knee bones from bi-planar x-ray images,” in *Machine Learning for Medical Image Reconstruction: Third International Workshop, MLMIR 2020, Held in Conjunction with MICCAI 2020, Lima, Peru, October 8, 2020, Proceedings* 3, pp. 123–133, Springer, 2020.
- [9] X. Ying, H. Guo, K. Ma, J. Wu, Z. Weng, and Y. Zheng, “X2ctgan: reconstructing ct from biplanar x-rays with generative adversarial networks,” in *Proceedings of the IEEE/CVF conference on computer vision and pattern recognition*, pp. 10619–10628, 2019.
- [10] Z. Liu, Y. Fang, C. Li, H. Wu, Y. Liu, Z. Cui, and D. Shen, “Geometry-aware attenuation field learning for sparse-view cbct reconstruction,” *arXiv preprint arXiv:2303.14739*, 2023.
- [11] Y. Lin, Z. Luo, W. Zhao, and X. Li, “Learning deep intensity field for extremely sparse-view cbct reconstruction,” *arXiv preprint arXiv:2303.06681*, 2023.
- [12] H. Zhao, Z. Zhou, F. Wu, D. Xiang, H. Zhao, W. Zhang, L. Li, Z. Li, J. Huang, H. Hu, et al., “Self-supervised learning enables 3d digital subtraction angiography reconstruction from ultra-sparse 2d projection views: a multicenter study,” *Cell Reports Medicine*, vol. 3, no. 10, 2022.
- [13] P. Bifulco, M. Cesarelli, R. Allen, M. Romano, A. Fratini, and G. Pasquariello, “2d-3d registration of ct vertebra volume to fluoroscopy projection: a calibration model assessment,” *EURASIP Journal on Advances in Signal Processing*, vol. 2010, pp. 1–8, 2009.
- [14] J. Alakuijala, U. Jaske, S. Sallinen, H. Hehminen, and J. Laitinen, “Reconstruction of digital radiographs by texture mapping, ray casting and splatting,” in *Proceedings of 18th Annual International Conference of the IEEE Engineering in Medicine and Biology Society*, vol. 2, pp. 643–645, IEEE, 1996.
- [15] B. Mildenhall, P. P. Srinivasan, M. Tancik, J. T. Barron, R. Ramamoorthi, and R. Ng, “Nerf: Representing scenes as neural radiance fields for view synthesis,” *Communications of the ACM*, vol. 65, no. 1, pp. 99–106, 2021.
- [16] D. Rückert, Y. Wang, R. Li, R. Idoughi, and W. Heidrich, “Neat: Neural adaptive tomography,” *ACM Transactions on Graphics (TOG)*, vol. 41, no. 4, pp. 1–13, 2022.
- [17] R. Zha, Y. Zhang, and H. Li, “Naf: neural attenuation fields for sparse-view cbct reconstruction,” in *International Conference on Medical Image Computing and Computer-Assisted Intervention*, pp. 442–452, Springer, 2022.
- [18] Y. Fang, L. Mei, C. Li, Y. Liu, W. Wang, Z. Cui, and D. Shen, “Snaf: Sparse-view cbct reconstruction with neural attenuation fields,” *arXiv preprint arXiv:2211.17048*, 2022.
- [19] Z. Zhou, H. Zhao, J. Fang, D. Xiang, L. Chen, L. Wu, F. Wu, W. Liu, C. Zheng, and X. Wang, “Tavivox: Time-aware attenuation voxels for sparse-view 4d dsa reconstruction,” *arXiv preprint arXiv:2309.02318*, 2023.
- [20] C. Sun, M. Sun, and H.-T. Chen, “Direct voxel grid optimization: Superfast convergence for radiance fields reconstruction,” in *Proceedings of the IEEE/CVF Conference on Computer Vision and Pattern Recognition*, pp. 5459–5469, 2022.
- [21] K. Gao, Y. Gao, H. He, D. Lu, L. Xu, and J. Li, “Nerf: Neural radiance field in 3d vision, a comprehensive review,” *arXiv preprint arXiv:2210.00379*, 2022.
- [22] A. Chen, Z. Xu, A. Geiger, J. Yu, and H. Su, “Tensorrf: Tensorial radiance fields,” in *European Conference on Computer Vision*, pp. 333–350, Springer, 2022.
- [23] T. Müller, A. Evans, C. Schied, and A. Keller, “Instant neural graphics primitives with a multiresolution hash encoding,” *ACM Transactions on Graphics (ToG)*, vol. 41, no. 4, pp. 1–15, 2022.
- [24] M. Niemeyer, J. T. Barron, B. Mildenhall, M. S. Sajjadi, A. Geiger, and N. Radwan, “Regnerf: Regularizing neural radiance fields for view synthesis from sparse inputs,” in *Proceedings of the IEEE/CVF Conference on Computer Vision and Pattern Recognition*, pp. 5480–5490, 2022.
- [25] M. Kim, S. Seo, and B. Han, “Infonerf: Ray entropy minimization for few-shot neural volume rendering,” in *Proceedings of the IEEE/CVF Conference on Computer Vision and Pattern Recognition*, pp. 12912–12921, 2022.
- [26] J. Yang, M. Pavone, and Y. Wang, “Freenerf: Improving few-shot neural rendering with free frequency regularization,” in *Proceedings of the IEEE/CVF Conference on Computer Vision and Pattern Recognition*, pp. 8254–8263, 2023.
- [27] P. Wang, L. Liu, Y. Liu, C. Theobalt, T. Komura, and W. Wang, “Neus: Learning neural implicit surfaces by volume rendering for multi-view reconstruction,” *arXiv preprint arXiv:2106.10689*, 2021.
- [28] Z. Li, T. Müller, A. Evans, R. H. Taylor, M. Unberath, M.-Y. Liu, and C.-H. Lin, “Neuralangelo: High-fidelity neural surface reconstruction,” in *Proceedings of the IEEE/CVF Conference on Computer Vision and Pattern Recognition*, pp. 8456–8465, 2023.
- [29] Y. Wang, Q. Han, M. Habermann, K. Daniilidis, C. Theobalt, and L. Liu, “Neus2: Fast learning of neural implicit surfaces for multi-view reconstruction,” in *Proceedings of the IEEE/CVF International Conference on Computer Vision*, pp. 3295–3306, 2023.
- [30] J. T. Barron, B. Mildenhall, M. Tancik, P. Hedman, R. Martin-Brualla, and P. P. Srinivasan, “Mip-nerf: A multiscale representation for anti-aliasing neural radiance fields,” in *Proceedings of the IEEE/CVF International Conference on Computer Vision*, pp. 5855–5864, 2021.
- [31] J. T. Barron, B. Mildenhall, D. Verbin, P. P. Srinivasan, and P. Hedman, “Mip-nerf 360: Unbounded anti-aliased neural radiance fields,” in *Proceedings of the IEEE/CVF Conference on Computer Vision and Pattern Recognition*, pp. 5470–5479, 2022.
- [32] W. Hu, Y. Wang, L. Ma, B. Yang, L. Gao, X. Liu, and Y. Ma, “Trimapr: Tri-mip representation for efficient anti-aliasing neural radiance fields,” in *Proceedings of the IEEE/CVF International Conference on Computer Vision*, pp. 19774–19783, 2023.
- [33] J. T. Barron, B. Mildenhall, D. Verbin, P. P. Srinivasan, and P. Hedman, “Zip-nerf: Anti-aliased grid-based neural radiance fields,” *arXiv preprint arXiv:2304.06706*, 2023.
- [34] A. Pumarola, E. Corona, G. Pons-Moll, and F. Moreno-Noguer, “D-nerf: Neural radiance fields for dynamic scenes,” in *Proceedings of the IEEE/CVF Conference on Computer Vision and Pattern Recognition*, pp. 10318–10327, 2021.
- [35] J. Fang, T. Yi, X. Wang, L. Xie, X. Zhang, W. Liu, M. Nießner, and Q. Tian, “Fast dynamic radiance fields with time-aware neural voxels,” in *SIGGRAPH Asia 2022 Conference Papers*, pp. 1–9, 2022.
- [36] S. Fridovich-Keil, G. Meanti, F. R. Warburg, B. Recht, and A. Kanazawa, “K-planes: Explicit radiance fields in space, time, and appearance,” in *Proceedings of the IEEE/CVF Conference on Computer Vision and Pattern Recognition*, pp. 12479–12488, 2023.
- [37] S. Park, M. Son, S. Jang, Y. C. Ahn, J.-Y. Kim, and N. Kang, “Temporal interpolation is all you need for dynamic neural radiance fields,” in *Proceedings of the IEEE/CVF Conference on Computer Vision and Pattern Recognition*, pp. 4212–4221, 2023.
- [38] A. C. Kak and M. Slaney, *Principles of computerized tomographic imaging*. SIAM, 2001.
- [39] W. E. Lorensen and H. E. Cline, “Marching cubes: A high resolution 3d surface construction algorithm,” in *Seminal graphics: pioneering efforts that shaped the field*, pp. 347–353, 1998.
- [40] Z. Wang, A. C. Bovik, H. R. Sheikh, and E. P. Simoncelli, “Image quality assessment: from error visibility to structural similarity,” *IEEE transactions on image processing*, vol. 13, no. 4, pp. 600–612, 2004.